



# Impact of hydration on the mechanical properties and damage mechanisms of natural silk fibre reinforced composites

Wenhan Tian<sup>a,b</sup>, Kang Yang<sup>a,c</sup>, Sujun Wu<sup>a</sup>, Jiping Yang<sup>a</sup>, Hongyun Luo<sup>a,b</sup>, Juan Guan<sup>a,b,\*</sup>, Robert O. Ritchie<sup>d,\*</sup>

<sup>a</sup> School of Materials Science and Engineering, Beihang University, Beijing 100191, China

<sup>b</sup> Beijing Advanced Innovation Center for Biomedical Engineering, Beijing 100083, China

<sup>c</sup> School of Materials Science and Engineering, Anhui University of Technology, Maanshan 243032, China

<sup>d</sup> Department of Materials Science and Engineering, University of California, Berkeley, CA 94720, United States

## ARTICLE INFO

### Keywords:

Natural fibers

Interface

Acoustic emission

Dynamic mechanical thermal analysis

## ABSTRACT

Silk fibres exhibit good biodegradability, biocompatibility and balanced strength and toughness, which are useful for toughness/impact-critical composites in the biomedical field. However, the impact of hydration has not been studied for silk fibre-reinforced polymers (SFRPs). In this work, SFRPs fabricated vacuum-assisted resin infusion (VARI) were treated under three hydration conditions. A hydration condition of 40 °C at 89% relative humidity (RH) was sufficient to induce a reduction in the tensile and flexural modulus and yield strength of SFRPs. Acoustic emission (AE) analysis showed that interface failure played a key role in the damage modes of SFRPs. Although mild hydration treatment appeared not to affect SFRPs, high hydration led to more susceptible interfacial failure. This work is intended to reveal the structural mechanisms of SRPPs under hydration, and to provide a useful reference for potential biomedical applications.

## 1. Introduction

There is a growing interest in employing natural fibres for fibre reinforced polymers (FRPs) owing to their biodegradability, low weight and competent mechanical performance [1–4]. Natural plant fibres such as flax, jute, ramie, sisal and bamboo, as reinforcement of composites, have become excellent alternatives to glass fibres and carbon fibres. Recently, natural silk fibres as single/hybrid fibre reinforcement have been utilized to improve the flexural mechanical properties and impact strength of FRPs [5–7]. For example, epoxy resin-based silk fibre reinforced plastics (SFRPs) display an excellent (sub-ambient) ductility at –50 °C, with simultaneous enhancements in impact strength and toughness when hybridized with carbon fibres [8,9]. SFRPs have been proposed as impact/toughness critical engineering materials [10–13] as they display a toughness that is higher than plant fibre reinforced plastics (PFRPs) and is comparable to glass fibre reinforced plastics (GFRPs) [14–16]. Thus, silk fibre reinforcement may bring forward new design freedoms and be suitable for specific applications such as composite biomedical devices [17,18].

Silk fibres are composed of micro- and nanofibrils, and the fibrils are

further composed of crystalline and amorphous regions. The chains in the crystalline region adopt a zigzag conformation, also called  $\beta$ -sheet conformation, whereas chains in the amorphous regions adopt random coil and helical structures that are often highly oriented. Such a semi-crystalline structure with a high degree of orientation makes most natural silk fibres ductile and tough, as distinct from stiff but brittle plant fibres.

Silk fibre produced by wild *Antheraea pernyi* (*A. pernyi*) exhibited > 45% tensile failure strain (twice of that of *Bombyx mori* (*B. mori*) silk), 5–15 GPa tensile modulus, and 400–600 MPa tensile strength [19], which make this silk extremely tough. As such, it has been proposed as an outstanding natural silk reinforcement and could be a silkworm silk substitute to the gold standard spider dragline silk [8]. The ductile and tough mechanical performance of silk can also be inherited by the composites SFRPs through the design of the matrices and the silk-matrix interface. Nevertheless, there remains challenges in comprehensively understanding the mechanical performance of SFRPs for actual industrial service and biomedical applications.

One concern is the humidity sensitivity of natural fibres when exposed to humid environments [20]. Indeed, understanding the water

\* Corresponding authors.

E-mail addresses: [juan.guan@buaa.edu.cn](mailto:juan.guan@buaa.edu.cn) (J. Guan), [roritchie@lbl.gov](mailto:roritchie@lbl.gov) (R.O. Ritchie).

<https://doi.org/10.1016/j.compositesa.2021.106458>

Received 6 January 2021; Received in revised form 19 April 2021; Accepted 2 May 2021

Available online 7 May 2021

1359-835X/© 2021 Elsevier Ltd. All rights reserved.

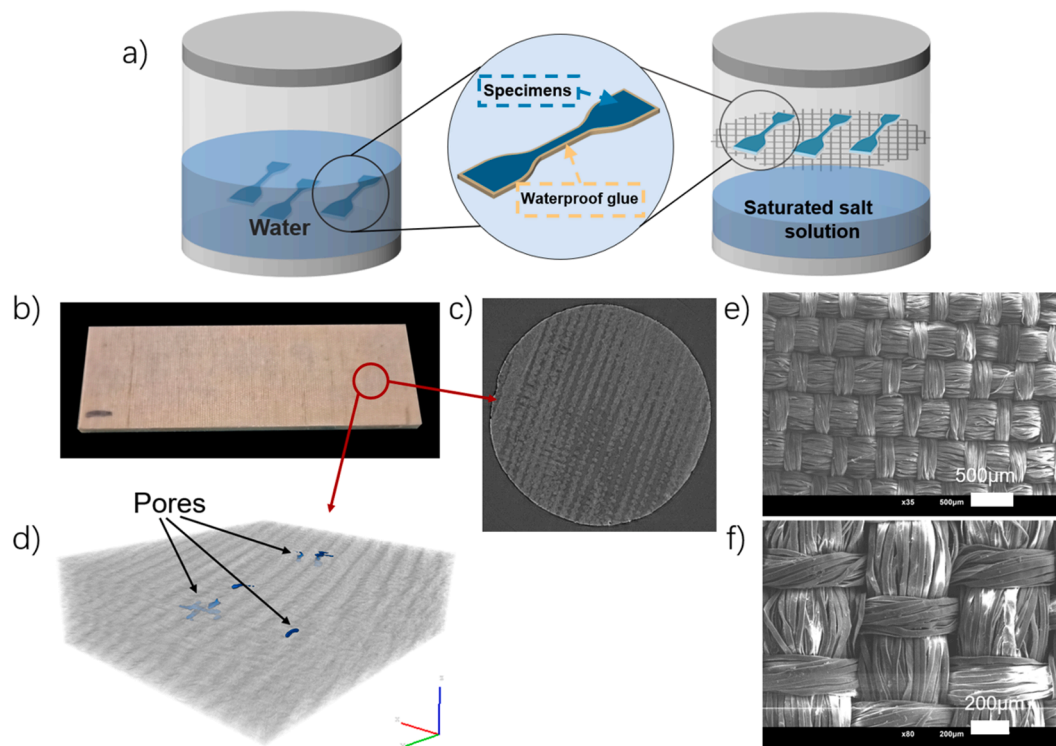


**Fig. 1.** Illustrations of the fabrication and hydration treatments. (a) The hydration treatment set-up for tensile specimens, with water immersion on the left and humidity treatment on the right. (b) Photograph of a SFRP specimen. (c) A slice image from the X-ray micro-tomography ( $\mu$ -CT) scan of the SFRP specimen. (d) A 3D volume image of the SFRP with noted pores reconstructed from the X-ray  $\mu$ -CT scan sliced images. (e, f) SEM images of the microstructure of the plain weave fabrics.

absorption or hydration behaviour of natural fibre composites and knowing their mechanical performance in a wet environment is essential for the structural applications of these composites.

In the past years, significant understanding has been gained on the mechanisms of moisture absorption in PFRPs. For example, water diffusion in PFRPs was shown to obey a modified Fick's law [21,22], and the stiffness, strength and dynamic mechanical properties of PFRPs were found to decrease markedly in humid environments [23–26]. Damaged interfaces between the plant fibre and matrix were found to be one major degradation mechanism, which resulted in poor stress transfer between the fibre and matrix [27]. Swelling and disorganization of the microfibril network with the plant fibres and plasticization of the matrix were also considered as important damage mechanisms in PFRPs [20]. However, the effects of moisture/hydration on the mechanical performance of SFRPs, have not been specifically studied.

In this work, SFRPs specimens were prepared from *A. pernyi* silk textiles and epoxy resin using vacuum-assisted resin infusion (VARI) based on an established methodology [9]. First, the water absorption behaviour of the SFRPs was investigated. Then the SFRPs were treated under three designed moisture/water conditions representing low/medium/high hydration conditions. After such controlled hydration treatments, the tensile and flexural mechanical properties of SFRPs were tested and analysed, prior to using acoustic emission and dynamic mechanical thermal analysis to investigate the salient damage mechanisms and hydration effects on the composites. This research is intended to improve our understanding of how environmental factors can affect the mechanical performance of natural silk fibre composites in light of the potential industrial and biomedical applications of these structural composites.

## 2. Materials and methods

### 2.1. Materials

Plain woven *A. pernyi* silk fabric was purchased from the Beijing Rui Fu Xiang Silk Store (Beijing, China). The silk fabric was plain-woven with  $\sim 110$  vertical fibres and  $\sim 30$  horizontal fibres in yarns. The areal density of silk fabric was  $1.35 \pm 0.10 \text{ kg}\cdot\text{m}^{-2}$ . The density of the silk was assumed as  $1300 \text{ kg}\cdot\text{m}^{-3}$  [28].

The epoxy resin system Araldite LY1564/Aradur3486 (epoxy resin/hardener) was manufactured by Huntsman Corporation (USA), with a curing ratio 1:0.34 by weight. The recommended curing procedure is  $80^\circ\text{C}$  for 8 hr with a cured epoxy resin with a density of  $\sim 1200 \text{ kg}\cdot\text{m}^{-3}$ . According to the manufacturer, the tensile modulus  $E_t$ , tensile strength  $\sigma_t$  and ultimate strain  $\varepsilon_t$  are  $3.0 \pm 0.1 \text{ GPa}$ ,  $73.4 \pm 0.2 \text{ MPa}$  and  $16.1 \pm 0.7\%$ , respectively [9].

### 2.2. Fabrication of composites

All SFRPs were fabricated as laminates using a tailor-made VARI set-up, followed by hot pressing in a steel frame with dimensions of  $250 \text{ mm} \times 150 \text{ mm} \times 2 \text{ mm}$ . In detail, fabrics were firstly dried in a vacuum oven at  $60^\circ\text{C}$  for 4 hr to remove water in the silk. 12 plies of silk fabric were then laid together to ensure a high fibre volume fraction of  $\sim 65\%$  in the composite. Then, the fabric piles were put into the vacuum bag with release paper, peel ply and infusion net. Pre-mixed uncured epoxy resin LY1564/Aradur3486 was infused driven by a vacuum pump-generated pressure to the vacuum bag for 15 min to fully impregnate the fabrics for hot press molding [9]. This was followed by hot pressing at a pressure of  $500 \text{ kPa}$  for 8 hr at  $80^\circ\text{C}$  until the curing reaction was complete.

### 2.3. Hydration treatments

Specimens for water infusion/absorption testing were cut into  $76.2 \times 25.4 \times 3.0$  mm rectangular blocks according to ASTM Standard 570 68 [29]. The cut sides of the specimens were sealed with Sharp's SRC1-93 glue. The water uptake was measured using an electronic balance with 0.1 mg resolution at intervals of 0, 3, 9, and 29 hr.

For mechanical test specimens, three different hydration conditions were chosen based on the ISO 4611: (i) 23 °C, immersed in water; (ii) 40 °C, in a relative humidity (RH) of 89% (produced by a saturated solution of potassium nitrate,  $\text{KNO}_3$ ); (iii) 40 °C, in a RH of 53% (produced by a saturated solution of sodium bromide, NaBr). As shown in Fig. 1(a), all treatments were conducted in sealed chambers at constant temperature. The weight uptake  $\Delta m$  (%) of the SFRPs specimens after hydration treatments for various times was calculated using the following equation:

$$\Delta m(\%) = \frac{m_t - m_0}{m_0} \times 100\% \quad (1)$$

where  $m_0$  represents the initial weight of the dry specimen, and  $m_t$  the weight of the treated specimens.

Using Fick's laws of diffusion to describe the water absorption behaviour for a rectangular specimen with uniform thickness and distribution, the relationship between weight increase and the square root of the diffusion time  $\sqrt{t}$  is given by [30,31]:

$$\frac{m_t}{m_\infty} = 4\sqrt{\frac{Dt}{\pi d^2}} \quad (2)$$

where  $m_\infty$  is the maximum water uptake at the equilibrium state,  $D$  is the diffusion coefficient and  $d$  is the thickness of specimen.

Tensile and flexural specimens were prepared according to the standards mentioned in the testing sections. SFRP specimens were treated for a maximum of 240 hr (10 days) under each hydration condition and taken out for testing at intervals of 12 hr, 16 hr, 24 hr, 48 hr, 96 hr (for tensile testing only) and 240 hr. Non-treated dry specimens were tested for comparison. At least 5 specimens were prepared for each hydration treatment to ensure that there were more than 3 sets of valid data.

### 2.4. Uniaxial tensile testing

Uniaxial tensile tests were performed on an Instron 8801 screw-driven testing machine (Instron Corp., Norwood, MA, USA) with a deformation rate of  $2 \text{ mm}\cdot\text{min}^{-1}$  according to the Chinese Standard GB/T 1040-92. It is noted that this testing method is designed for plastics without fibre reinforcements; it is thus not the ideal testing standard for orthogonal fibre reinforced plastics. Therefore, the tensile mechanical properties obtained in this study may deviate somewhat from those from a different standard. The strains were measured using an extensometer (Instron, Catalogue no. 2620-601). The tensile test specimens were dog bone-shaped with dimensions of  $115 \text{ mm} \times 25 \text{ mm} \times 2 \text{ mm}$  and a gauge length of 70 mm. Specimens were subject to different hydration treatments before tensile testing. At least 5 specimens were tested repeatedly for each treatment to ensure that there were more than 3 sets of valid data. The representative stress-strain curves were chosen as the middle curve of the measurements with standard deviations calculated at representative points.

A yarn of the *A. pernyi* silk fibre was aligned and fixed in the custom-cut paper frame. Uniaxial tensile tests were performed on a Zwick Line Z0.5 materials testing machine (Z0.5, Zwick/Roell., Germany) with a deformation rate of  $2 \text{ mm}\cdot\text{min}^{-1}$ . The silk fiber was straightened with minimum force before the test. The strain was calculated by dividing the original length by the displacement of the silk fibre yarn.

### 2.5. Flexural testing

Flexural tests were conducted at a deformation rate of  $2 \text{ mm}\cdot\text{min}^{-1}$  in accordance with Chinese Standard GB/T1449-2005 on a mechanical testing machine with a 10 kN load cell (SANS, MTS Industrial System Co. Ltd., China). The testing specimens were cut to  $30 \times 15 \times 2$  mm dimensions, with the span-to-depth ratio set to 12. Specimens were subject to different hydration treatments before flexural testing. Similarly, at least 5 specimens were tested repeatedly for each treatment, and ensure that there were more than 3 sets of valid data. The flexural modulus and the strength (corresponding to the yield stress) of SFRPs were calculated and compared.

The flexural stress  $\sigma_f$  and the flexural strain  $\epsilon_f$  of the SFRPs specimens were calculated using the following equations:

$$\sigma_f = \frac{3FL}{2bd^2} \quad (3)$$

$$\epsilon_f = \frac{6Dd}{L^2} \quad (4)$$

In (3), (4)  $\sigma_f$  is the stress in the outer surface at midpoint, MPa.  $F$  is the load at a given point on the load-deflection curve,  $L$  is the support span,  $b$  is the width of specimen and  $d$  is the depth of the specimen,  $\epsilon_e$  is the strain in the outer surface,  $D$  is the maximum deflection of the center of the specimen. The flexural modulus of the SFRPs specimens was calculated using the tangent modulus of elasticity, which is the ratio of stress to corresponding strain in the elastic limit.

### 2.6. Dynamic mechanical thermal analysis (DMTA)

Dynamic mechanical thermal analysis was performed with a dynamic mechanical analyzer (DMA) Q800 (TA Instrument, Waters Ltd.). The dimensions of the rectangular test specimens were  $10 \times 2$  mm with a length-to-thickness ratio of 5. The tests were run in a three-point bending mode at a frequency of 1 Hz and dynamic deformation strain of 0.1%. The temperature was ramped from the room temperature to  $180 \text{ °C}$  at  $3 \text{ °C}\cdot\text{min}^{-1}$ .

### 2.7. X-ray computed microtomography ( $\mu$ -CT)

Imaging of SFRPs was performed at the BL13W1 beam line in Shanghai Synchrotron Radiation Facility (SSRF, China). The energy of the X-ray was fixed to 18 KeV; a detector with the spatial resolution of  $6.5 \mu\text{m}$  was chosen within a field of view of 13 mm. About 1200 radiographs were taken at regular increments over  $180^\circ$  of rotation. The sectional images were first reconstructed using the PITRE3 software; 3D images were then reconstructed using the Avizo software.

### 2.8. Morphology analysis

To evaluate the microstructure and morphology of the silk composites, specimens with/without hydration treatments were observed in the scanning electron microscope (SEM, JEOL JSM-6010, Japan) before and after mechanical testing. The target surfaces were sputter-coated with gold for 2 min. SEM images were taken at 14 kV accelerating voltage under the secondary electron imaging mode.

### 2.9. Acoustic emission (AE)

During the flexural deformation of the SFRPs, AE signals were recorded by an AE win v2.19 AE system (Physical Acoustic Corporation, USA) with a digital signal processor. The AE system was calibrated before each test using the procedure of breaking a standard pencil lead to ensure good induction of AE signals between the composite and the sensors. The lead was placed at the edge of the flexural specimen, and the received AE signals ( $>90 \text{ dB}$ ) recorded. One piezoelectric sensor

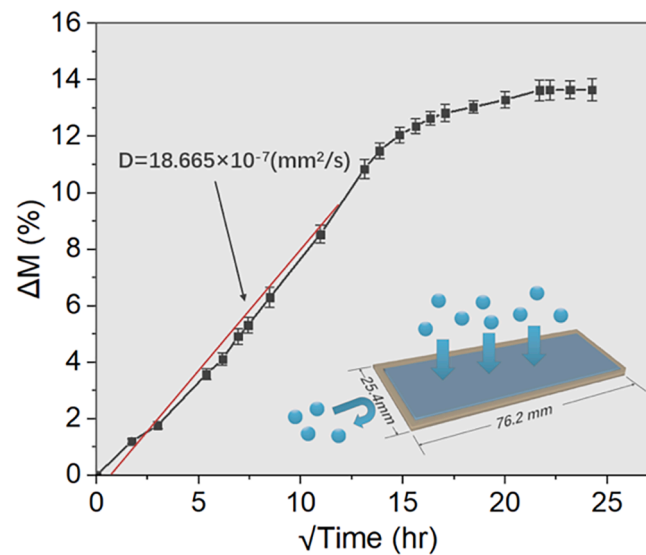


**Fig. 2.** Water uptake behaviour, in terms of weight gain as a function of the square root of time, for SFRPs under water. Inset is a schematic diagram of the specimen with its sides sealed by glue for hydration test.

(Nano-30) with frequency range of 100 kHz–1 MHz, a resonant frequency of 140 kHz and a preamplifier with 40 dB gain was used to capture the AE signals. The piezoelectric sensor was attached on the face of the SFRP specimens with silicone grease. The set-up is shown in Fig. 8(a). To filter acoustic signals coming from the test machine or other external sources, an amplitude acquisition threshold of 40 dB was used in the experiments.

### 3. Results and discussion

#### 3.1. Water absorption

In Fig. 2, the variation in water uptake as a function of  $\sqrt{t}$  is given for SFRPs immersed in water. Initially, the linear growth of water uptake follows Fick's law perfectly with a diffusion coefficient of  $D = 1.8 \times 10^{-6}$  ( $\text{mm}^2 \cdot \text{s}^{-1}$ ), before it slowly approaches the equilibrium condition. The estimated diffusion coefficient ( $D$ ) of water in SFRPs is in a similar range to that reported for flax fibre reinforced polymer composites with comparable fibre volumes [30,31]. These properties provide the possibility of future use of silk fibres. This behaviour suggests that, similar to plant fibres, silk fibres are hydrophilic to a certain degree. In addition, absorbed water could also induce the fibrillation of micro fibres in the *A. pernyi* silk fibre, which is known to be a feature of wild silkworm silks and has been observed after hydration.

#### 3.2. Effect of hydration on the mechanical properties of SFRPs

Before examining the effect of hydration, the consistency of the preparation process for SFRPs by VARI and hot pressing was assessed. Specimens from the same preparation batch displayed remarkably reproducible tensile behaviour. In Fig. 1(c,d) from X-ray computed microtomography, the silk fabric can be seen to tightly pack within the matrix. The estimated porosity in the SFRPs was  $< 0.03$  vol%, which proved the fabrication methods via VARI were effective to ensure consistency and to eliminate defects such as voids and bubbles.

Three hydration treatments were applied as described in section 2.3. The first treatment of 40 °C at 53% RH represents a relatively mild humid environment (*i.e.*, similar to the climate and weather conditions in the summer of northern China), 40 °C at 89% RH represents a highly humid environment, and 23 °C water immersion represents a wet or water-saturated condition and thus the most severe hydration.

Fig. 3(a-c) shows typical tensile engineering stress–strain curves of the SFRPs with different hydration treatments. All the curves exhibit three stages: elastic deformation, yielding and plastic deformation to failure. The yield strength, tensile strength and elongation after hydration treatment are normalized with respect to their initial dry values and are plotted in Fig. 3(d-f). Dry specimens exhibit an average yield strength of 96.3 MPa, a tensile strength of 145.2 MPa, and tensile (Young's) modulus of 6.02 GPa with an elongation of 15.4%. The first treatment at 40 °C at 53% RH for 10 days only slightly decreased the tensile strength by 2.4% to 141.7 MPa, whereas the yield strength and tensile modulus even marginally increased to 98.8 MPa and 6.79 GPa, respectively. The second treatment (40 °C at 89% RH) resulted in much larger reduction in the yield stress, tensile modulus and tensile strength, corresponding to 51.8 MPa (46.3% lower), 3.66 GPa (60.8% lower) and 123.3 MPa (84.9% lower), respectively. The water immersion treatment for 10 days further reduced the yield stress to 23.7 MPa (75.4% lower) and the strength to 51.6 MPa (46.4% lower). At the same time, the elongation in all SFRP specimens after hydration treatments increased by a maximum of 70%. For example, the second treatment for 10 days and the water immersion treatment for 10 days led to 28% and 70% increase in elongation at break compared to the dry samples. As a measure of the toughness calculated from the area under the stress–strain curves, the variation in tensile breaking energy, shown in Fig. 3(h), did not change significantly with the hydration treatment and time, in contrast to the variations in strength and breaking strain. Such a trend in the tensile breaking energy may inspire prediction methods for tensile properties of SFRPs subject to hydration treatments.

Fig. 4 compares the tensile fracture morphology of dry and fully hydrated SFRPs. In Fig. 4(a-d), various tensile damage modes of hydrated SFRPs are evident, including fibre and fibre yarn pull-out, matrix cracking, fibrillation of micro fibres and fibre–matrix interface damage. Fig. 4(c) indicates good interfacial bonding between silk and the epoxy matrix. In Fig. 4(e), the fibre yarn pull-out of the dry specimens appeared to be more severe, leading to rougher fracture surface compared with the hydrated specimens. It also showed more micro-fibrillation of silk fibres for the dry SFRPs.

In Fig. 5(a-c), SFRP specimens under flexural tests can be seen to exhibit yielding at the maximum flexural stress, which is often defined as flexural strength for ductile specimens. Our SFRPs did not actually fracture owing to the excellent ductility of the silk and epoxy resin. Thus, we were only able to compare the flexural modulus and flexural yield

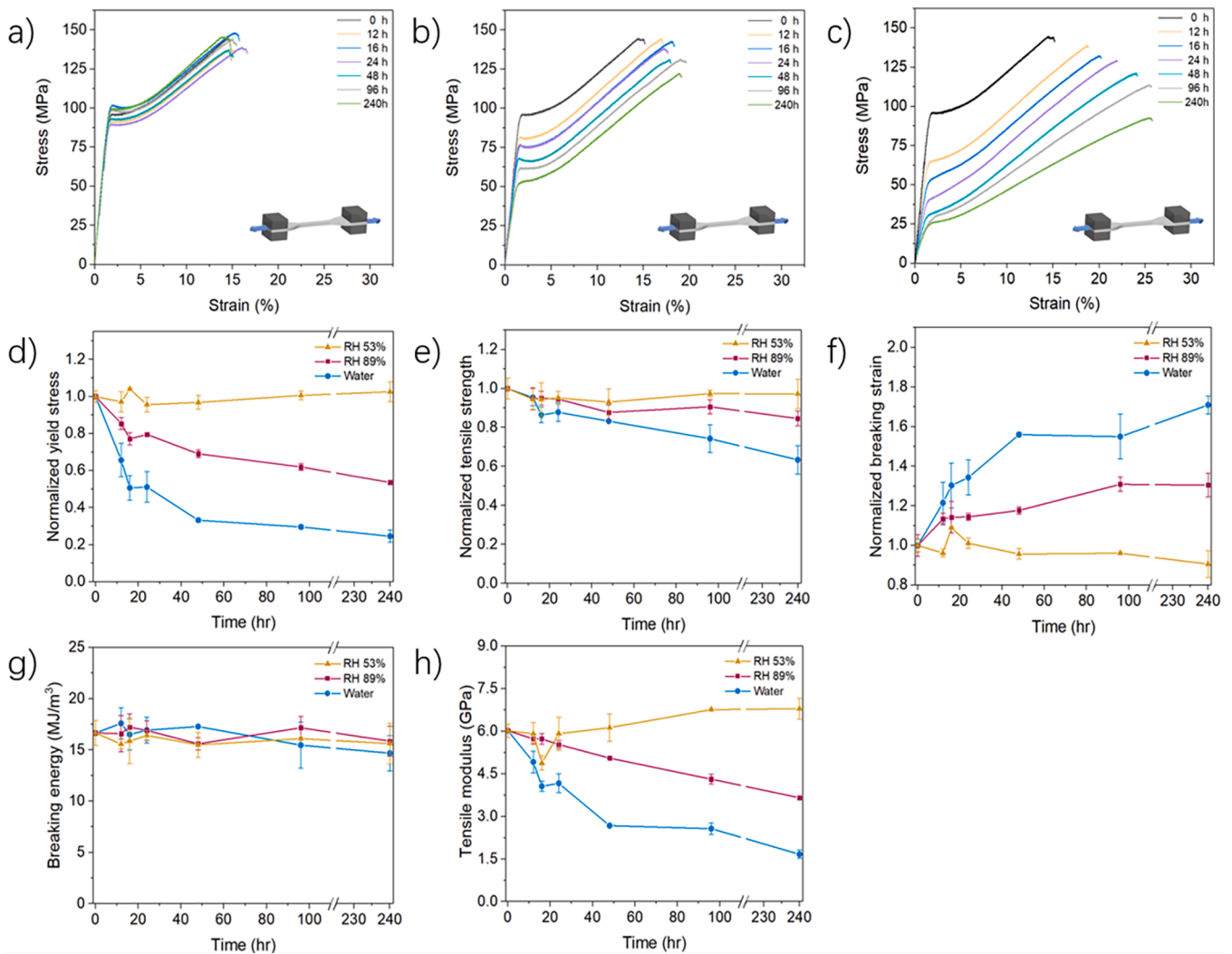


**Fig. 3.** Uniaxial tensile mechanical properties of control and hydrated SFRPs. (a-c) Typical tensile engineering stress–strain curves of SFRPs after different hydration conditions: (a) 40 °C at 53% RH; (b) 40 °C at 89% RH; (c) 23 °C water immersion. (d-f) Summarized results of the tensile mechanical properties of the SFRPs including (d) yield strength, (e) tensile strength, (f) elongation, (g) Young's modulus, and (g) breaking energy. The number of tested specimens for each condition is 5.

stress. As shown in Fig. 5d, the flexural strength of the SFRPs showed similar trends with hydration to that of the tensile strength and modulus. Notably, low hydration leads to increased flexural strength, which agreed with the results in another study on pure epoxy resin treated under 75% RH [32].

The surface morphologies of the dry and mildly hydrated specimens after flexural testing are compared in Fig. 6(a-d). For the dry specimen with a rougher upper surface, many cracks are deflected from the tensile direction, and transverse cracks can be seen. The numbers of cracks within the same area ( $2000 \mu\text{m}^2$ ) in Fig. 6(a,b) turned out to be similar. However, these cracks in dry specimens appeared much smaller and narrower although the edges of these cracks were rougher. In contrast, the hydrated SFRPs displayed larger-sized cracks.

### 3.3. Dynamic mechanical thermal analysis

The glass transition behaviour of the epoxy resin in SFRPs after hydration may reflect changes in the epoxy resin-fibre interface properties [33,34]. When a glassy amorphous polymer is heated, it transitions to a rubbery state through the glass transition. Dynamic mechanical thermal analysis or DMTA is a powerful tool to analyse the glass transition behavior of the matrix in the composite [19,35]. The storage modulus at

the low temperature region from Fig. 7 (a,c) for the hydration treated specimens are comparable with the tensile elastic modulus from Fig. 3 (h). The decreasing trend of storage modulus at the same temperature is similar to that of tensile modulus.

The loss tangent  $\tan\delta$  defines the ratio of the loss modulus over the storage modulus, which indicates the damping/dissipation of the polymer. One definition of the glass transition temperature  $T_g$  is the  $\tan\delta$  peak position temperature. The  $T_g$ s of the SFRPs after the medium and high hydration treatments are compared in Fig. 7. The  $T_g$  for the dry SFRP was 93.2 °C. After the 96 hr hydration treatment, the  $T_g$  decreased by 4.0 °C to 89.2 °C for 40 °C at 89% RH treatment (Fig. 7(b)) and by 8.6 °C to 84.6 °C for water immersion treatment (Fig. 7(d)). This result indicates that the adhesion between the epoxy resin matrix and silk fibres becomes impaired by mobile water molecules after the hydration treatment. Such a decrease is consistent with the observed reduction in the tensile/flexural modulus and strength of the composite. In addition, the observed increase in the  $\tan\delta$  peak for SFRPs after hydration indicates that the epoxy resin matrix may have become plasticized by the water [33].

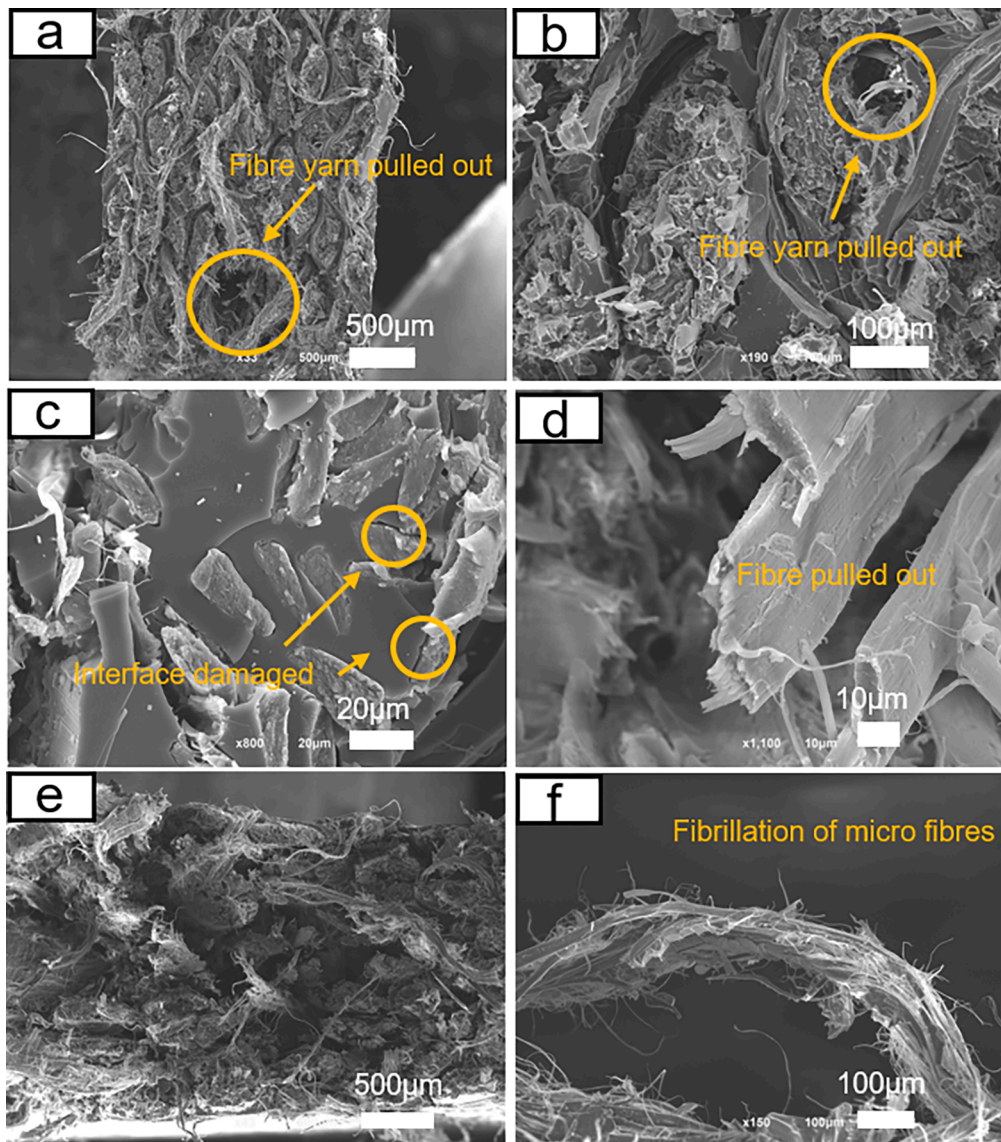


Fig. 4. SEM images of tensile fracture morphologies. (a, b, c, d) Treated SFRPs at 23 °C in water for 96 hr. (e, f) Dry SFRP specimens.

### 3.4. Damage modes analysis with acoustic emission

Acoustic emission (AE) techniques are a useful non-destructive analytical tool to identify damage and failure modes after hygro-thermal aging in FPRs [36,37]. Specifically, the frequency and/or amplitude signals of acoustic events can be correlated with various failure processes, such as matrix fracture, fibre–matrix interface debonding, fibre pull-out and fibre fracture [38–40]. The acoustic measurements can be coupled with mechanical tests under various deformation modes (e.g., tensile or flexural) to provide real-time information on the structural and morphological changes in the composite [41,42]. For example, Czigány *et al.* utilized AE techniques to identify the origin of AE signals (specifically the amplitude) to provide correlations with the damage modes, e.g., delamination and fibre pull-out, in basalt fibre reinforced composites [36].

To calibrate the AE responses, prior to assessing the effect of hydration, the characteristic damage modes in dry/original SFRPs were first identified, using pure epoxy resin and two SFRPs specimens (2.0 and 3.6 mm thick). In the flexural test, the flexural strength showed a significant increase with increased thickness or decreased length-to-thickness ratio. This is because when the flexural load is stronger than

the friction caused by the large flexural deformation, the downward movement of the loading will cause the specimen to slide on the supports [43]. Under the same flexural deformation, the far side from the contact surface to the roller of the thicker specimen will be subjected to a much larger tensile stress and shear stress, such that fibre fracture, interfacial debonding and delamination is more prone to occur [43]. We also subjected pure silk fibre yarn to uniaxial tensile testing to identify the AE signals for fracture of pure silks.

The main AE signals to correlate with the damage modes in composites are amplitude, frequency and energy. Related studies [44,45] demonstrated that the frequency signal was more tightly correlated with versatile damage modes such as matrix cracking, fibre fracture and interfacial debonding. Here we studied the frequency signals for the damage modes in SFRPs. Fig. 8 shows a comparison of the peak frequency signals from our AE measurements. Considering first the constituents of the composite, the pure epoxy resin exhibited concentrated AE events with low peak frequencies in the 20–50 kHz range after yield, which we believe is associated with cracking of the resin [38]. The cracks and rough surfaces shown in Fig. 6(e, f) are consistent with the AE signals in the epoxy resin. There are also scattered signals in the higher frequency range of 175–275 kHz, which may be attributed to unstable

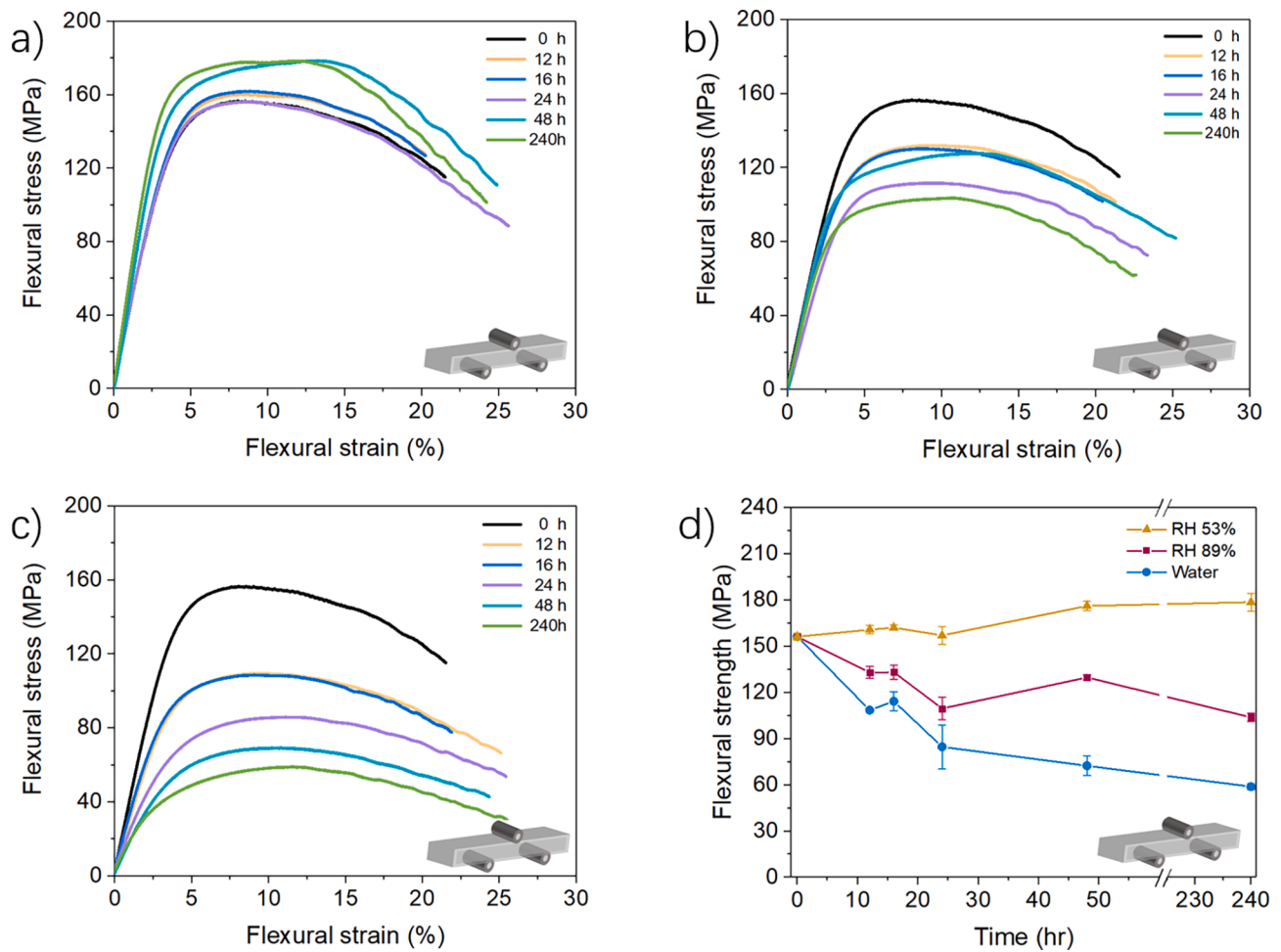


**Fig. 5.** Flexural mechanical properties of control and hydrated SFRPs. (a-c) Typical flexural stress–strain curves of SFRPs after different hydration conditions: (a) 40 °C at 53% RH; (b) 40 °C at 89% RH; (c) 23 °C water immersion; (d) Summarized flexural strength of SFRPs as a function of treatment time. The number of tested specimens for each condition is 5.

crack growth in the epoxy resin [38]. In Fig. 8(c), AE signals from the tensile deformation of the silk fibres appeared above 250 kHz and are concentrated in a single narrow frequency range (290–310 kHz) following the yield point and close to fracture on the stress–strain curve. There is some overlap in the peak frequency signals in the 250–275 kHz range from both the silk fibres and the epoxy resin. Fig. 8(d, e) displays the corresponding characteristic AE signals from the SFRPs. The 2-mm thick specimens, that were not fractured after flexural testing, displayed only scattered signals in the 100–250 kHz range. For the thicker SFRP specimens, a large number of signals in the 20–350 kHz range appeared. Most new AE signals in the 100–250 kHz were not seen for the silk fibres or epoxy resin and can be attributed to characteristic damage modes in the composite, *i.e.*, fibre–matrix debonding and fibre pull-out. The featured AE signals centered at 150 kHz frequency range was deemed to be associated with interfacial damage. In terms of the sequence of AE events, the signals for such interfacial damage appeared early in the test, followed by further damage in the matrix and the fibres. After flexural testing, microcracks along the fibres can be seen in Fig. 6 (g, h) from the side view of the thin SFRP specimen close to the most tensioned surface of the specimen. For the thicker specimen, fibre breakages corresponding to > 250 kHz AE signals and interface damage corresponding to 100–250 kHz AE signals were prevalent, as shown in Fig. 6(i, j). These damage morphologies correspond well with the AE signals in Fig. 8. The final classification of AE signals for SFRPs is summarized in Fig. 8(f).

The SFRPs in this work all failed in a ductile mode. When the first AE

signal is recorded by the sensor, the dry/untreated SFRPs may even reach a flexural strain of 2.5%. Following these AE experiments on dry specimens, the damage processes in the hydrated SFRPs were investigated under flexural deformation with real time AE measurements. The flexural stress–strain curves with indications of the peak frequency signals after hydration treatments of 12 hr and 240 hr are summarized in Fig. 9. Compared with the dry SFRPs, the signals of all the hydrated specimens became more scattered, especially for the specimens immersed in water. Notably, the AE events also started earlier, especially for the interface failure. Although a few higher frequency signals further appeared (*i.e.*, ~310 kHz for 53% RH and 240 hr; ~350 kHz for water immersion and 240 hr), which may be related to fibre fracture, the AE signals were mostly concentrated in 100–250 Hz for the interface damage. This agrees with the DMTA analysis. Taken together, these results strongly suggest that interfacial damage remained the dominant damage mechanism in hydrated SFRPs, which further may have triggered other damage modes of damage which included fibre fracture.

### 3.5. Water interactions with silk and epoxy resin in SFRPs

Silk fibres possess a distinct structural hierarchy from that of plant-based natural fibres [46–48]. Although the primary structure or the amino acid sequence of different animal silks is not the same, all silks share a similar  $\beta$ -sheet conformation structure and crystalline-amorphous two-phase condensed structure. Water can plasticize silk to reduce the stiffness as well as to increase the ductility of silk by

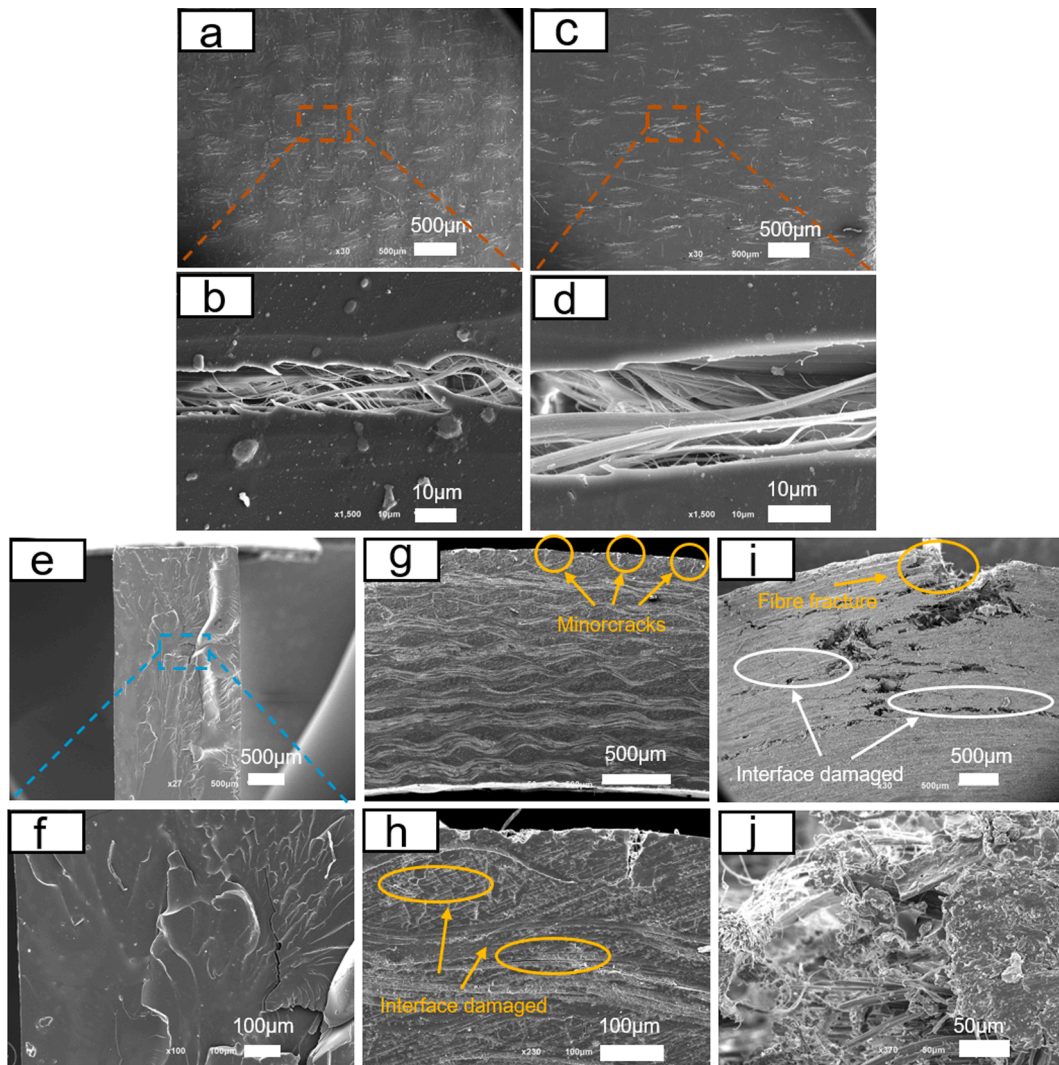


**Fig. 6.** SEM of the morphology of the pure epoxy resin and SFRP specimens after flexural testing. (a, b) Upper surface of dry SFRPs specimens. (c, d) Upper surface of treated SFRPs at 40 °C at 53% RH for 240 hr. (e, f) Fracture surfaces of the epoxy resin. (g, h) Side surface of the thin SFRP specimen (2 mm thickness), and (i, j) side surface of thick SFRP specimen (3.6 mm thickness).

permeating into its amorphous structure, causing water-induced glass transition in silk [20]. As epoxy resin is highly cross-linked and hydrophobic, the extent of water absorption and swelling is negligible compared with silk [49]. Although water may facilitate post-curing of epoxy resin in some cases [32], the epoxy resin that was already fully cured in this study should not further develop crosslinking.

The hydration condition of 40 °C at 89% RH was well above that of 25 °C at 80% RH, which is a critical condition to induce the glass transition in *A. pernyi* silk [20]. Thus, the water-plasticization of silk should contribute to the modulus reduction in SFRPs. Moreover, in the interface of the SFRPs after hydration, silk fibres tend to swell and soften, but the matrix restricts such relaxation. Therefore, at the fibre–matrix interface, shear stresses may be created. Fig. 10 demonstrates such a mechanism. In our case, when the hydration was mild, such interfacial stresses may repair some defects (*i.e.*, voids) at the interface and lead to improved yield strength. When the hydration was high, the interfacial stresses begin to damage the fibre–matrix adhesion, contributing to a significantly reduced modulus and strength of SFRPs. Such a mechanism is consistent with the damage mode analysis from AE results in Fig. 9.

#### 4. Conclusions

In this work we have investigated the effect of hydration on the mechanical properties and damage mechanisms of *Antheraea pernyi* silk fibre reinforced epoxy resin composites (*Ap*-SFRPs). Three hydration conditions (40 °C at 53% RH, 40 °C at 89% RH, and 23 °C immersed in water for 10 days / 240 hr) were applied. After the low hydration treatment, the yield strength of SFRPs could be enhanced; whereas after the high hydration treatment the plasticization of silk fibres as well as the deteriorated interface led to significantly reduced tensile/flexural strength/modulus. Dynamic mechanical thermal analysis (DMTA) confirmed such weakened interface adhesion.

Acoustic emission (AE) analysis was used to reveal the sequence and contributions of the damage modes in the SFRPs. Matrix failure and interface debonding dominated the failure of the dry composites, whereas interfacial damage was far more prevalent in the highly hydrated SFRPs. Plasticization of silk fibres and the interfacial stresses due to the mismatched behaviour of silk and epoxy resin under hydration were deemed to cause the property reduction in SFRPs. This study can provide important guidelines for the application of such natural fibre-based composites for structural applications where hydration may be a problem.

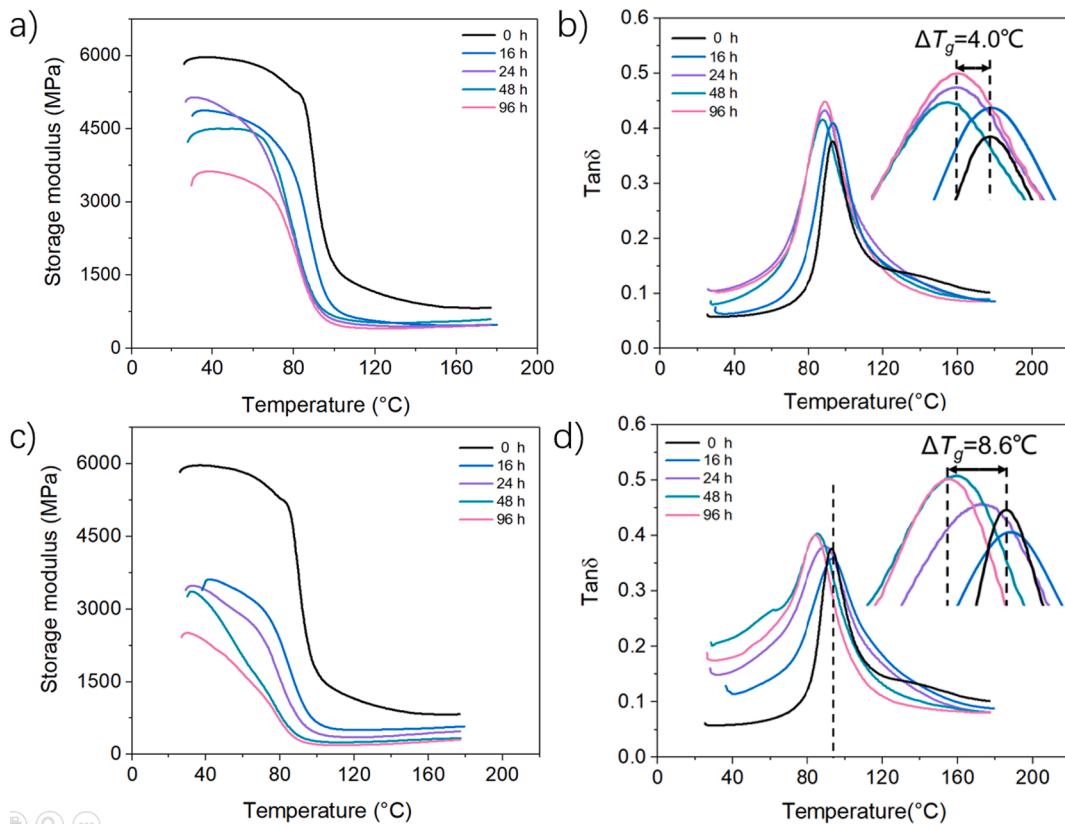


**Fig. 7.** Dynamic mechanical thermal analysis of SFRPs from 25 °C to 180 °C after the three hydration treatments. (a, c) The storage modulus ( $E'$ ) of specimens treated at 40 °C at 89% RH and at 23 °C in water for various periods, and (b, d) the damping factor  $\tan\delta$  of the two differently treated specimens.

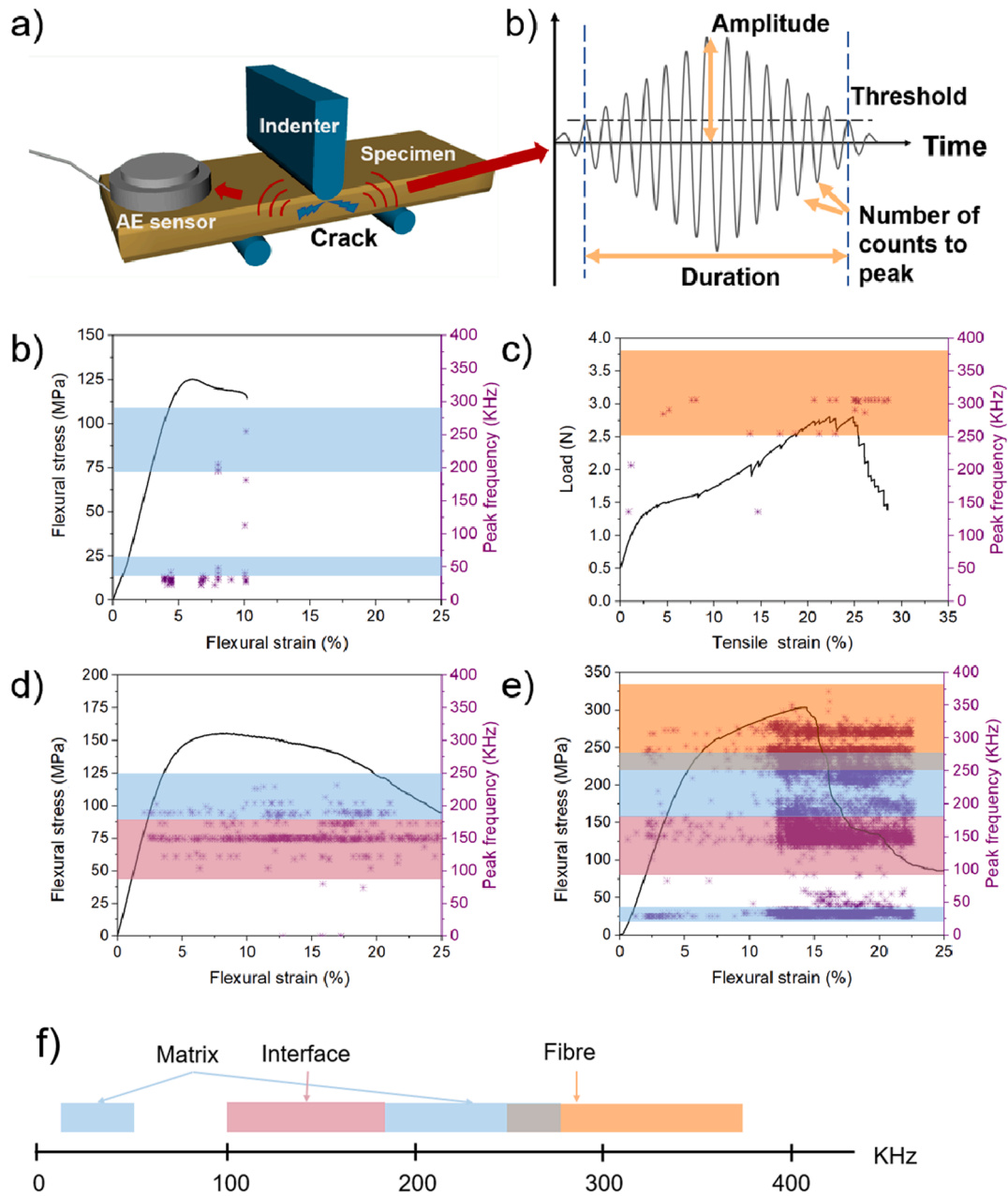


**Fig. 8.** Representative engineering stress–strain behaviour and real-time acoustic emission (AE) peak frequency signals of the matrix, fibre and composites. (a) Illustration of the AE set-up and the signal characteristics. (b) Pure epoxy resin under flexural load, (c) single silk fibre yarn under tensile load, (d) thin SFRP specimen under flexural load, (e) thick SFRP specimen under flexural load, and (f) classification result of AE signals.

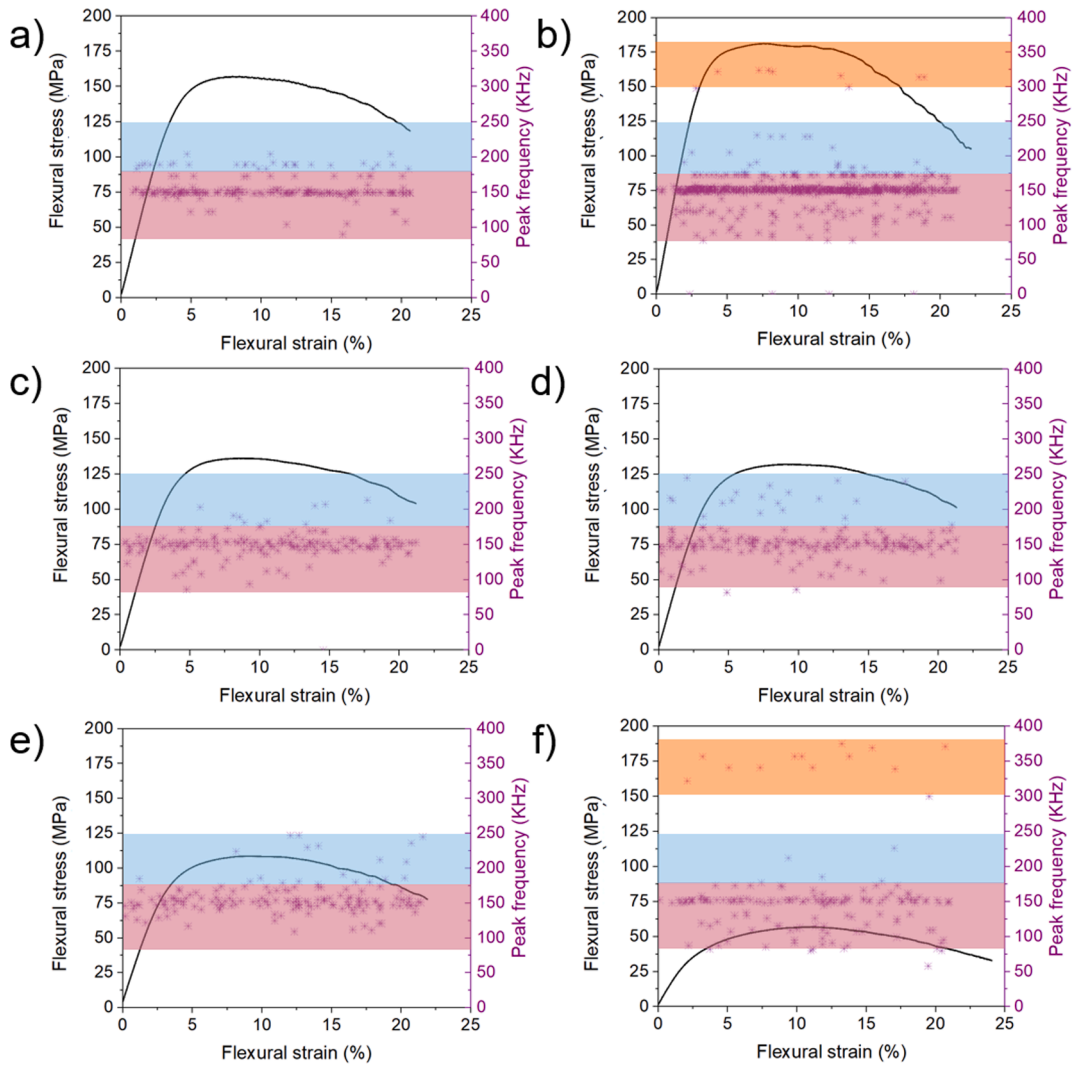


**Fig. 9.** Typical flexural stress–strain curves and real-time AE frequency signals (classified according to Fig. 8(f)) of SFRPs after hydration treatments for 12 hr or 240 hr. (a) and (b) 40 °C at 53% RH; (c) and (d) 40 °C at 89% RH; (e) and (f) 23 °C water immersion. (a), (c) and (e) correspond to 12 hr; (b), (d) and (f) correspond to 240 hr.

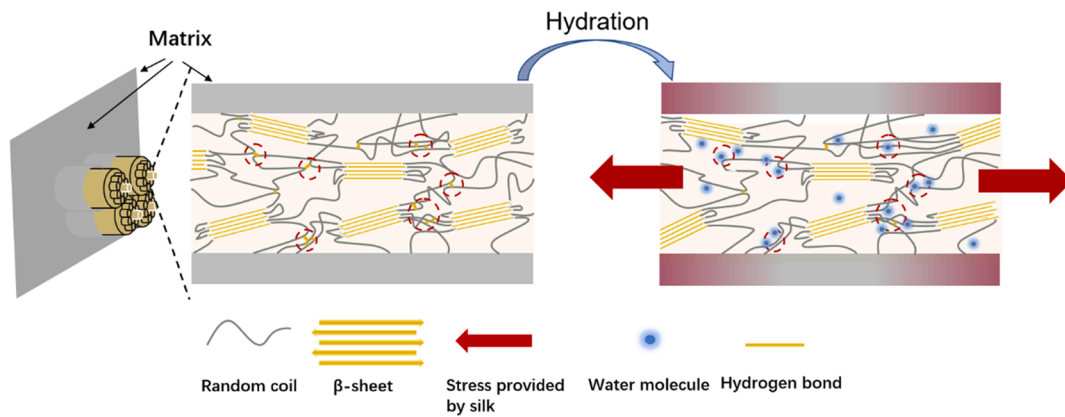


**Fig. 10.** Schematics of structure changes of SFRPs before and after hydration treatment.

## Declaration of Competing Interest

The authors declare that they have no known competing financial interests or personal relationships that could have appeared to influence the work reported in this paper.

## Acknowledgments

This study was funded by National Natural Science Foundation of China [grant number 51905019] and China Postdoctoral Science Foundation [grant numbers 2019M650432 and 2020T130041]. The authors are grateful to Shanghai Synchrotron Radiation Facility (BL13W1 Beam line).

## References

- [1] Dayo AQ, Gao BC, Wang J, Liu WB, Derradji M, Shah AH, et al. Natural hemp fiber reinforced polybenzoxazine composites: curing behavior, mechanical and thermal properties. *Compos Sci Technol* 2017;144:114–24.
- [2] Kumar N, Das D. Fibrous biocomposites from nettle (*Girardinia diversifolia*) and poly(lactic acid) fibers for automotive dashboard panel application. *Compos Part B-Eng* 2017;130:54–63.
- [3] Lau KT, Hung PY, Zhu MH, Hui D. Properties of natural fibre composites for structural engineering applications. *Compos Part B-Eng* 2018;136:222–33.
- [4] Safri SNA, Sultan MTH, Jawaid M, Jayakrishna K. Impact behaviour of hybrid composites for structural applications: a review. *Compos Part B-Eng* 2018;133:112–21.
- [5] Ude AU, Ariffin AK, Azhari CH. An experimental investigation on the response of woven natural silk fiber/epoxy sandwich composite panels under low velocity impact. *Fiber Polym* 2013;14(1):127–32.
- [6] Khanam PNR, Mohan M, Raghu K, John K, Naidu SV. Tensile, flexural and Compressive properties of sisal/silk hybrid composites. *J Reinf Plast Compos* 2007.
- [7] Shah DU, Porter D, Vollrath F. Opportunities for silk textiles in reinforced biocomposites: Studying through-thickness compaction behaviour. *Compos Part a- Appl S* 2014;62:1–10.
- [8] Yang K, Guan J, Numata K, Wu CG, Wu SJ, Shao ZZ, et al. Integrating tough *Antheraea pernyi* silk and strong carbon fibres for impact-critical structural composites. *Nat Commun* 2019;10.
- [9] Wu CG, Yang K, Gu YZ, Xu J, Ritchie RO, Guan J. Mechanical properties and impact performance of silk-epoxy resin composites modulated by flax fibres. *Compos Part a-Apppl S* 2019;117:357–68.
- [10] Shah DU, Porter D, Vollrath F. Can silk become an effective reinforcing fibre? A property comparison with flax and glass reinforced composites. *Compos Sci Technol* 2014;101:173–83.
- [11] Shao ZZ, Vollrath F. Materials: Surprising strength of silkworm silk. *Nature*. 2002; 418(6899):741.
- [12] Rockwood DN, Preda RC, Yucel T, Wang XQ, Lovett ML, Kaplan DL. Materials fabrication from Bombyx mori silk fibroin. *Nat Protoc*. 2011;6(10):1612–31.
- [13] Ho MP, Wang H, Lee JH, Ho CK, Lau KT, Leng JS, et al. Critical factors on manufacturing processes of natural fibre composites. *Compos Part B-Eng*. 2012;43(8):3549–62.
- [14] Eshkoor RA, Ude AU, Sulong AB, Zulkifli R, Ariffin AK, Azhari CH. Energy absorption and load carrying capability of woven natural silk epoxy-triggered composite tubes. *Compos Part B-Eng* 2015;77:10–8.
- [15] Yang K, Ritchie RO, Gu YZ, Wu SJ, Guan J. High volume-fraction silk fabric reinforcements can improve the key mechanical properties of epoxy resin composites. *Mater Des* 2016;108:470–8.
- [16] Yang K, Wu SJ, Guan J, Shao ZZ, Ritchie RO. Enhancing the mechanical toughness of epoxy-resin composites using natural silk reinforcements. *Sci Rep-Uk* 2017;7.
- [17] Li G, Li Y, Chen GQ, He JH, Han YF, Wang XQ, et al. Silk-based biomaterials in biomedical textiles and fiber-based implants. *Adv Healthc Mater* 2015;4(8):1134–51.
- [18] de Moraes MA, Beppu MM. Biocomposite membranes of sodium alginate and silk fibroin fibers for biomedical applications. *J Appl Polym Sci* 2013;130(5):3451–7.
- [19] Wang Y, Guan J, Hawkins N, Porter D, Shao ZZ. Understanding the variability of properties in *Antheraea pernyi* silk fibres. *Soft Matter* 2014;10(33):6321–31.
- [20] Fu CJ, Porter D, Shao ZZ. Moisture effects on *Antheraea pernyi* silk's mechanical property. *Macromolecules* 2009;42(20):7877–80.
- [21] Pomes B, Derue I, Lucas A, Nguyen JF, Richaud E. Water ageing of urethane dimethacrylate networks. *Polym Degrad Stabil* 2018;154:195–202.
- [22] Liu W, Hoa SV, Pugh M. Water uptake of epoxy-clay nanocomposites: model development. *Compos Sci Technol* 2007;67(15–16):3308–15.
- [23] Cadu T, Van Schoors L, Sicot O, Moscardelli S, Divet L, Fontaine S. Cyclic hygrothermal ageing of flax fibers' bundles and unidirectional flax/epoxy composite. Are bio-based reinforced composites so sensitive? *Ind Crop Prod* 2019; 141.
- [24] Jiang N, Yu T, Li Y. Effect of hydrothermal aging on injection molded short jute fiber reinforced poly(lactic acid) (PLA) composites. *J Polym Environ*. 2018;26(8): 3176–86.
- [25] Le Duigou A, Davies P, Baley C. Seawater ageing of flax/poly(lactic acid) biocomposites. *Polym Degrad Stabil* 2009;94(7):1151–62.
- [26] Moudood A, Rahman A, Khanlou HM, Hall W, Ochsner A, Francucci G. Environmental effects on the durability and the mechanical performance of flax fiber/bio-epoxy composites. *Compos Part B-Eng* 2019;171:284–93.
- [27] Joffre T, Segerholm K, Persson C, Bardage SL, Hendriks CLL, Isaksson P. Characterization of interfacial stress transfer ability in acetylation-treated wood fibre composites using X-ray microtomography. *Ind Crop Prod*. 2017;95:43–9.
- [28] Lewin M. Handbook of fiber chemistry. 3rd ed. Boca Raton: CRC/Taylor & Francis; 2007.
- [29] Venkateshwaran N, ElayaPerumal A, Alavudeen A, Thiruchitrabalam M. Mechanical and water absorption behaviour of banana/sisal reinforced hybrid composites. *Mater Design*. 2011;32(7):4017–21.
- [30] Munoz E, Garcia-Manrique JA. Water absorption behaviour and its effect on the mechanical properties of flax fibre reinforced bioepoxy composites. *Int J Polym Sci*. 2015;2015.
- [31] Scida D, Assarar M, Poilane C, Ayad R. Influence of hygrothermal ageing on the damage mechanisms of flax-fibre reinforced epoxy composite. *Compos Part B-Eng* 2013;48:51–8.
- [32] Lettieri M, Frigione M. Effects of humid environment on thermal and mechanical properties of a cold-curing structural epoxy adhesive. *Constr Build Mater* 2012;30: 753–60.
- [33] Gu H. Dynamic mechanical analysis of the seawater treated glass/polyester composites. *Mater Des* 2009;30(7):2774–7.
- [34] Saba N, Jawaid M, Alothman OY, Paridah MT. A review on dynamic mechanical properties of natural fibre reinforced polymer composites. *Constr Build Mater* 2016;106:149–59.
- [35] Duc F, Bourban PE, Plummer CJG, Manson JAE. Damping of thermoset and thermoplastic flax fibre composites. *Compos Part A – Appl S* 2014;64:115–23.
- [36] Czigan T. Special manufacturing and characteristics of basalt fiber reinforced hybrid polypropylene composites: Mechanical properties and acoustic emission study. *Compos Sci Technol* 2006;66(16):3210–20.
- [37] Hu YH, Lang AW, Li XC, Nutt SR. Hygrothermal aging effects on fatigue of glass fiber/polydicyclopentadiene composites. *Polym Degrad Stabil* 2014;110:464–72.
- [38] Monti A, El Mahi A, Jendli Z, Guillaumat L. Mechanical behaviour and damage mechanisms analysis of a flax-fibre reinforced composite by acoustic emission. *Compos Part A – Appl Sci* 2016;90:100–10.
- [39] Ramirez-Jimenez CR, Papadakis N, Reynolds N, Gan TH, Purnell P, Pharaoh M. Identification of failure modes in glass/polypropylene composites by means of the primary frequency content of the acoustic emission event. *Compos Sci Technol* 2004;64(12):1819–27.
- [40] Sause MGR, Muller T, Horoschenkoff A, Horn S. Quantification of failure mechanisms in mode-I loading of fiber reinforced plastics utilizing acoustic emission analysis. *Compos Sci Technol* 2012;72(2):167–74.
- [41] Kumar CS, Arumugam V, Santulli C. Characterization of indentation damage resistance of hybrid composite laminates using acoustic emission monitoring. *Compos Part B-Eng* 2017;111:165–78.
- [42] Maillat E, Morscher GN. Waveform-based selection of acoustic emission events generated by damage in composite materials. *Mech Syst Signal Pr* 2015;52–53: 217–27.
- [43] Li HG, Xu YW, Hua XG, Liu C, Tao J. Bending failure mechanism and flexural properties of GLARE laminates with different stacking sequences. *Compos Struct* 2018;187:354–63.
- [44] Chen GW, Luo HY, Wu SJ, Guan J, Luo J, Zhao TS. Flexural deformation and fracture behaviors of bamboo with gradient hierarchical fibrous structure and water content. *Compos Sci Technol* 2018;157:126–33.
- [45] Gutkin R, Green CJ, Vangrattanachai S, Pinho ST, Robinson P, Curtis PT. On acoustic emission for failure investigation in CFRP: Pattern recognition and peak frequency analyses. *Mech Syst Signal Pr* 2011;25(4):1393–407.
- [46] Wang Y, Wen JC, Peng B, Hu BW, Chen X, Shao ZZ. Understanding the mechanical properties and structure transition of *antheraea pernyi* silk fiber induced by its contraction. *Biomacromolecules* 2018;19(6):1999–2006.
- [47] Chen HY, Mao MH, Ding X. Influence of moisture absorption on the interfacial strength of bamboo/vinyl ester composites. *Compos Part A - Appl Sci* 2009;40(12): 2013–9.
- [48] Li Y, Xie L, Ma H. Permeability and mechanical properties of plant fiber reinforced hybrid composites. *Mater Des* 2015;86:313–20.
- [49] Chow WS. Water absorption of epoxy/glass fiber/organo-montmorillonite nanocomposites. *Express Polym Lett* 2007;1(2):104–8.